remote sensing

MDPI

Article

The Combination Application of FY-4 Satellite Products on Typhoon Saola Forecast on the Sea

Chun Yang *, Bingying Shi and Jinzhong Min

Key Laboratory of Meteorological Disaster of Ministry of Education (KLME)/Joint International Research Laboratory of Climate and Environment Change (ILCEC)/Collaborative Innovation Center on Forecast and Evaluation of Meteorological Disaster (CIC-FEMD), Nanjing University of Information Science & Technology, Nanjing 210044, China; 20211101023@nuist.edu.cn (B.S.); minjz@nuist.edu.cn (J.M.)

* Correspondence: yangchun@nuist.edu.cn

Abstract: Satellite data play an irreplaceable role in global observation data systems. Effective comprehensive application of satellite products will inevitably improve numerical weather prediction. FengYun-4 (FY-4) series satellites can provide not only radiance data but also retrieval data with high temporal and spatial resolutions. To evaluate the potential benefits of the combination application of FY-4 Advanced Geostationary Radiance Imager (AGRI) products on Typhoon Saola analysis and forecast, two group of experiments are set up with the Weather Research and Forecasting model (WRF). Compared with the benchmark experiment, whose sea surface temperature (SST) is from the National Centers for Environmental Prediction (NCEP) reanalysis data, the SST replacement experiments with FY-4 A/B SST products significantly improve the track and precipitation forecast, especially with the FY-4B SST product. Based on the above results, AGRI clear-sky and all-sky assimilations with FY-4B SST are implemented with a self-constructed AGRI assimilation module. The results show that the AGRI all-sky assimilation experiment can obtain better analyses and forecasts. Furthermore, it is proven that the combination application of AGRI radiance and SST products is beneficial for typhoon prediction.

Keywords: Fengyun satellite; all-sky assimilation; sea surface temperature; combination application

check for updates

Citation: Yang, C.; Shi, B.; Min, J. The Combination Application of FY-4 Satellite Products on Typhoon Saola Forecast on the Sea. *Remote Sens.* **2024**, *16*, 4105. https://doi.org/10.3390/rs16214105

Academic Editor: Gang Zheng

Received: 11 September 2024
Revised: 25 October 2024
Accepted: 1 November 2024
Published: 2 November 2024

Copyright: © 2024 by the authors. Licensee MDPI, Basel, Switzerland. This article is an open access article distributed under the terms and conditions of the Creative Commons Attribution (CC BY) license (https://creativecommons.org/licenses/by/4.0/).

1. Introduction

As one of the major disastrous weather systems worldwide, typhoons, especially those making landfall, usually can result in significant damage, injury, and loss of life [1,2]. Therefore, in order to minimize the societal and economic impacts, it is essential to make accurate typhoon forecasts that allow for the early tracking of approaching typhoons.

Advanced numerical weather prediction (NWP) has been the most useful way to predict the track and intensity of a typhoon [3–5]. However, forecast errors are typically unavoidable in NWP systems. And, errors in initial conditions are one of the main sources of forecast errors. Previous studies have also found that typhoon forecasts are sensitive to initial conditions in the NWP model [6,7]. Therefore, improving the accuracy of initial conditions, not only the atmospheric condition but also the ocean condition, is a vital requirement for the improvement of typhoon numerical forecasts. Nevertheless, typhoons commonly occur over open oceans, where conventional observations are limited [8]. Thus, the high temporal and spatial resolution satellite observations, which can provide useful information in marine areas, have become indispensable role in providing more accurate initial conditions and, consequently, improving typhoon numerical predictions [9].

The data assimilation technique is one of the keys to improving initial atmospheric conditions. Various types of satellite data, such as the retrieval of atmospheric temperature profiles [10] and atmospheric motion vectors [11,12], have been used to better represent atmospheric information and improve forecasts. Furthermore, since Eyre et al. [13] directly assimilated the satellite radiance data with the variational data assimilation method, the

direct assimilation of satellite radiance data, from different satellites and different sensors, has become the major application for satellite data assimilation [14]. And, many meteorologists have proved the advantages of direct satellite radiance assimilation in improving typhoon analyses and forecasts [15–18]. Especially, all-sky satellite assimilation schemes bring more cloud information in numerical prediction, which further improves typhoon forecasts [16,18].

Sea surface temperature (SST) is a vital factor in driving the surface wind speed, providing immense heat and moisture, and generating the pressure gradient in the boundary layer [19]. Therefore, it is one of the important exogenous forcings in the NWP systems. And, a large number of studies are available about its impacts on the genesis [20], movement [21,22], and intensification [23,24] of typhoons. Thus, apart from the initial atmospheric condition, the accurate representation of SST in the initial ocean boundary condition is also of crucial importance for typhoon forecasts. As one source of SST data, satellite-derived SST products have a larger cover area and high temporal and spatial resolutions. Some meteorologists have replaced the model initial SST with satellite-derived SST and found improvements in the intensity, track, and precipitation of typhoon predictions [25,26].

The Fengyun-4 (FY-4) series is the second-generation geostationary meteorological satellite of China. This series has launched a trial satellite, FY-4A, and an operational satellite, FY-4B. The Advanced Geostationary Radiance Imager (AGRI) is one of the primary instruments onboard FY-4 satellites. Compared with the Visible and Infrared Spin Scan Radiometer (VISSR) on the last geostationary satellite series, FY-2, AGRI has a wider spectral range and higher temporal and spatial resolutions [27]. Thus, it can provide products with high qualities and high resolutions, such as the level 1 radiance data, the retrieved SST products, and cloud-type data. Reasonable integration and application of these satellite data should inevitably improve the forecast of typhoons and other weather systems.

Former studies have evaluated different satellite SST products, such as the Tropical Rainfall Measuring Mission (TRMM) satellite, the Geostationary Operational Environmental Satellite (GOES), and the Meteorological Operational Satellite (Metop), and estimated the impact of AGRI assimilation in NWP [25,26,28–32]. However, the quality of SST products from FY-4 A/B has not been investigated yet, and the universal impact of AGRI radiance assimilation, especially all-sky assimilation, still needs to be proven. Furthermore, the combination application of satellite products from FY-4 series satellites on numerical weather prediction of typhoons has not been assessed either.

In this study, in order to evaluate the potential benefit of AGRI products on improving typhoon simulation, the AGRI radiances and SST data are used to provide more accurate initial conditions in the Weather Research and Forecasting model (WRF) based on Super Typhoon Saola, which was one of the most powerful tropical cyclones in the South China Sea on record, causing extensive damages in China and the Philippines. The impact of AGRI SST data on the Saola forecast is assessed to explore the applicability of AGRI-retrieved SST in improving ocean boundary conditions. Further, the clear-sky and all-sky AGRI radiance data assimilation experiments are conducted with a self-constructed module to give a more realistic representation of the atmosphere, and their benefits in Saola prediction are also investigated.

The rest of this paper is organized as follows. Section 2 briefly introduces the AGRI products and the new AGRI assimilation module configurations. Section 3 provides an overview of Typhoon Saola and the influences of AGRI SST data on typhoon simulation, followed by the results of AGRI radiance direct assimilation in Section 4. Finally, the conclusions and discussions are summarized in Section 5.

2. Materials and Methods

2.1. The AGRI Dataset

The level 1 radiance data and the corresponding GEO data for AGRI onboard FY-4A are used for assimilation, with 4 km spatial resolution every 15 min. FY-4A/AGRI

has 14 spectral bands ranging from visible to long-wave infrared, with two water vapor channels centered at 6.25 and 7.1 μm, respectively [27]. These two channels mainly provide information on moisture at middle and high levels of the atmosphere, which is important for typhoon simulation. In Figure 1, it also can be seen that the weighting function peaks of the two channels are located around 350 hPa and 400 hPa, while channels 11–13 are near the ground and channel 14's peak is at 750 hPa. Following the previous studies, two water vapor channels, channels 9–10, are applied in the assimilation experiments. Additionally, when AGRI radiance data are introduced in assimilation experiments, a thinning mesh of 60 km is adopted.

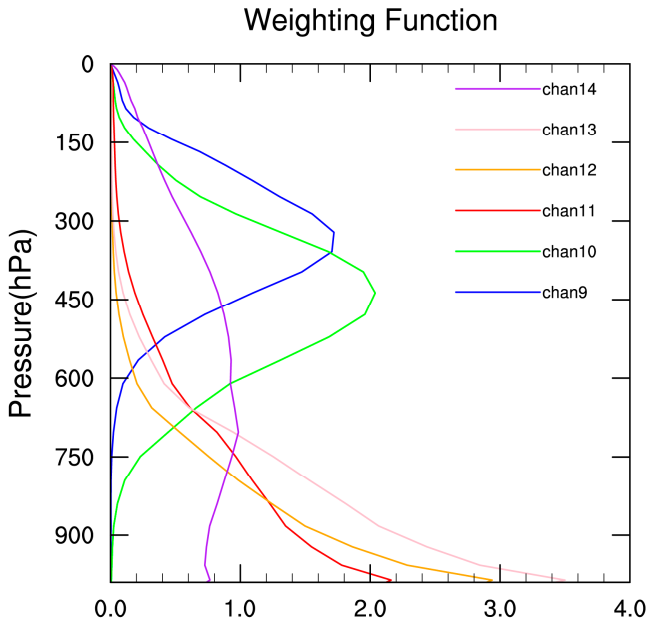


Figure 1. The weighting function of channels 9-14 of FY-4A AGRI with RTTOV and the U.S. standard atmospheric profile.

FY-4B/AGRI has the same coverage range, spectral range, spatial resolution, and temporal resolution as FY-4A/AGRI. However, compared with the AGRI onboard FY-4A, FY-4B adjusts and optimizes the spectral bandwidth of some channels and adds another low-level water vapor channel in the 7.24–7.60 μm band. In addition, the calibration accuracy of the infrared channels improved from better than 1.0 K to better than 0.7 K.

The level 2 SST products used in this study are retrieved from AGRI split-window bands onboard FY-4A and FY-4B, respectively. He et al. [33,34] have demonstrated that SST from FY-4B is more accurate than that from FY-4A. The spatial resolutions of those products are both 4km. The FY-4A SST products are available every 15 min [35]. For FY-4B, there are several SST retrieval products with different time resolutions. Considering the data coverage and quality, the daily mean SST product is selected in this study.

2.2. Data Assimilation System Configuration

The data assimilation system used in our study is the Weather Research and Forecasting Data Assimilation (WRFDA) version 4.4. The three-dimensional variational (3DVAR) scheme is employed to provide an improved estimate of the actual atmospheric state through minimizing a scalar cost function. The cost function $J(\mathbf{x})$ can be written as follows [36]:

$$J(\mathbf{x}) = \frac{1}{2}(\mathbf{x}-\mathbf{x_b})^{\mathrm{T}}\mathbf{B}^{-1}(\mathbf{x}-\mathbf{x_b}) + \frac{1}{2}\times(\mathbf{y}-H(\mathbf{x}))^{\mathrm{T}}\mathbf{O}^{-1}(\mathbf{y}-H(\mathbf{x})) \quad (1)$$

where $\mathbf{x}$ and x_b are the atmospheric state vector and the background field, respectively. $\mathbf{B}$ is the background error covariance, y is the observation field, $\mathbf{O}$ is the observation error

covariance, H is the observation operator, and $(\ )^{\mathbf{T}}$ indicates a transpose. **B** is computed by the National Meteorological Center (NMC) method [37] by taking 24 h and 12 h forecasts from 15 August to 15 September 2023. The five standard control variables, including eastward velocity, northward velocity, temperature, surface pressure, and pseudo relative humidity, are applied.

The FY-4A AGRI clear-sky and all-sky assimilation module was first configurated in WRFDA with radiative transfer for the TIROS Operational Vertical Sounder (RTTOV). The level 1 product of AGRI was read in HDF (Hierarchical Data Format). The unique observation error model, bias correction, and quality control methods for FY-4A AGRI clear-sky and all-sky assimilation were implemented in the new assimilation module.

The forward model of version 12.3 of RTTOV serves as the observation operator to simulate clear and cloudy radiances, while the tangent-linear and adjoint operators of RTTOV are included to compute the Jacobians. Apart from the temperature and moisture profiles used as the inputs for clear-sky radiance simulations, extra hydrometeor inputs are introduced for AGRI all-sky radiance simulations [38]. Because of additional hydrometeor inputs for RTTOV in the all-sky assimilation system, the simulated results in cloudy and rainy areas are more precise than in the clear-sky assimilation system. Thus, extra observations in areas covered by clouds can be assimilated in an all-sky assimilation system. In addition, the Jacobians of brightness temperature (BT) with respect to hydrometeors from the adjoint radiative transfer model are temporarily neglected for all-sky assimilation. Hence, different from the standard all-sky data assimilation scheme, the scheme employed in this study is a pseudo-all-sky data assimilation method without hydrometeor control variables [39].

For clear-sky AGRI radiance data assimilation, the observation error is set to 1.5 K for channels 9 and 10 based on the long-time statistic. When assimilating all-sky radiances, the symmetric error model developed by Okamoto [40] is applied to estimate the observation error for channels 9–10. In this model, the observation error is assigned by an averaged cloud amount parameter CA and is expressed as

$$CA = \frac{|B - B_{clr}| \ + \ |O - B_{clr}|}{2} \tag{2}$$

where B and O are the AGRI all-sky BTs from background and observation, respectively, and B_{clr} is defined as the AGRI background clear-sky BT simulation without cloud effects. Then, the observation error can be decided by the following:

$$SD = \begin{cases} SD_{min} \ CA \le CA_1 \\ SD_{min} \ + \ \frac{SD_{max} - SD_{min}}{CA_2 - CA_1}(CA - CA_2) \ CA_1 < CA < CA_2 \\ SD_{max} \ CA \ge CA_2 \end{cases} \tag{3}$$

where SD_{min} represents the observation error in clear-sky regions defined by the threshold CA_1 and SD_{max} is the observation error in fully cloudy areas as defined by CA_2. The values of the above four parameters in this study are set following the values in Shi et al. [38].

The Variational Bias Correction (VarBC) method [41,42] is also applied in this study to reduce bias when assimilating radiance data from AGRI. The bias correction predictors used for clear-sky assimilation are a constant component, 1000–300 hPa and 200–50 hPa layer thicknesses, surface skin temperature, total column water vapor, and the sine of the satellite zenith angle and its square and cube. Especially, for all-sky assimilation, the average CA between channels 9 and 10 is employed as an additional predictor to correct cloudy radiance biases at these two channels.

The quality control (QC) schemes for AGRI clear-sky assimilation are as follows: (1) gross observation check; (2) rejecting observations with zenith angles over 60°; (3) dismissing observations when the absolute values of bias-corrected observation minus background (OMB) exceed three times the observation errors; and (4) only reserving observations flagged as clear with FY-4A/AGRI L2-level cloud mask products (CLMs).

Owing to the more accurate simulated results in cloudy and rainy areas in the all-sky assimilation system, apart from observations flagged as clear, observations in other areas can also be used for assimilation. The QC procedures for all-sky radiance assimilation, except for step 4, are the same as in clear-sky assimilation. Additionally, the observations are rejected when *CA* is larger than 10 K and 15 K at channels 9 and 10, respectively, owing to large OMB standard deviation and significant fluctuation over these thresholds.

3. Impacts of AGRI SST Products on Typhoon Saola Simulations

3.1. Overview of Typhoon Saola

According to the Japan Meteorological Agency (JMA) record (Figure 2), Saola formed as a tropical depression over the western North Pacific on 22 August 2023. In the following five days, it moved westwards slowly and cycled around over the seas east of Luzon (Figure 2a). Its intensity increased rapidly during this period, with a maximum wind (MW) of 95 knots and a central sea level pressure (CSLP) of 940 hPa at 1800 UTC on 26 August (Figure 2b). It then continued to move westwards and entered the South China Sea. On August 30, it intensified to a super typhoon, with an MW of 105 knots and a CSLP of 920 hPa. Afterward, it gradually approached the coast of Guangdong and made landfall on September 2. Because of the frictional consumption, it weakened continuously and disappeared at 1200 UTC on 3 September in the sea around Guangdong.

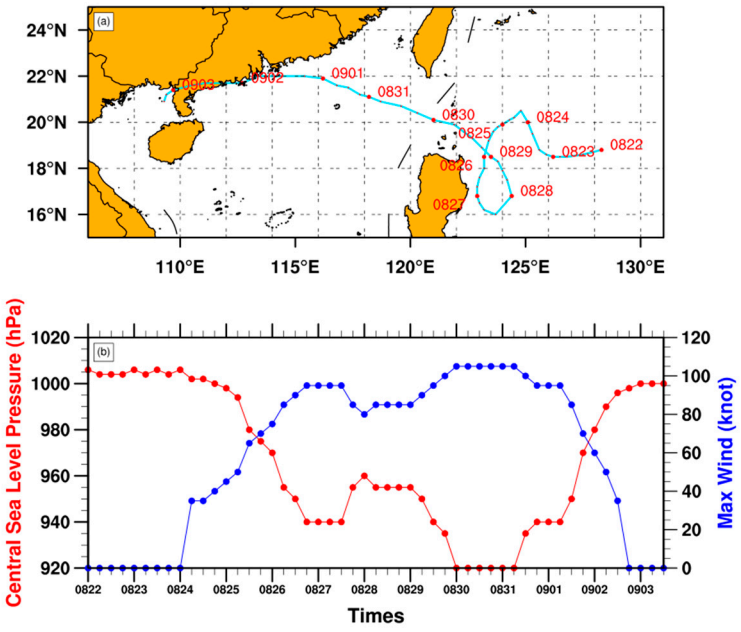


Figure 2. (**a**) The evolution of the best track, (**b**) the central sea level pressure (units: hPa) and maximum wind (units: knot) for Typhoon Saola from 0000 UTC 22 August to 1200 UTC 3 September 2023.

3.2. Experimental Design

Version 4.4 of the Weather Research and Forecasting (WRF) Advanced Research WRF (ARW) model is applied for Typhoon Saola prediction [43]. The landfall process of Typhoon Saola from 0600 UTC on 30 August to 1200 UTC on 2 September 2023 is selected for simulation.

The simulation domain for the WRF model is approximately from 5°N to 40°N and from 100°E to 145°E, with 9 km 601 × 451 horizontal grids and 41 vertical levels up to 50 hPa. The time step is 20 s. The initial and boundary conditions are from the National Centers for Environmental Prediction (NCEP) reanalysis data with a 6 h interval and 0.25° × 0.25° horizontal resolution. The parameterization scheme settings include WSM6 microphysics, RRTM long wave radiation physics, RRTMG short wave radiation physics,

the MM5 similarity scheme for near-surface-layer process, the Noah scheme for land surface, and the Yonsei University (YSU) boundary layer physics.

Three parallel experiments are conducted first to investigate the quality of AGRI SST data on model boundary condition representation and its impacts on the Saola forecast (Table 1). The experiment with the original SST data from NCEP data is conducted as the benchmark experiment named "*CON*". Two experiments named "SSTA" and "SSTB" are performed, respectively. SSTA replaces the SST data with the 5-day mean SST data retrieved from AGRI onboard FY-4A, while the second experiment SSTB modifies the initial SST data with the 5-day mean SST from FY-4B.

Table 1. The experimental design of SST modification experiments.

Name	Description
CON	The original SST from NCEP data
SSTA	The 5-days-mean SST from FY-4A
SSTB	The 5-days-mean SST from FY-4B

The 5-day mean AGRI SST is merged from 25th to 29th August. The original SST is used over the area where satellite SST data are missing. A nine-point average smoothing is applied for the AGRI SST data to ensure the continuity of the SST data. In Figure 3, it is clear that the original SST in *CON* is higher than SSTA and SSTB over the South China Sea and the sea east of Taiwan, while SSTA is lower than SSTB. Because of the distribution of SST, three experiments obtained different track and intensity forecasts of Typhoon Saola.

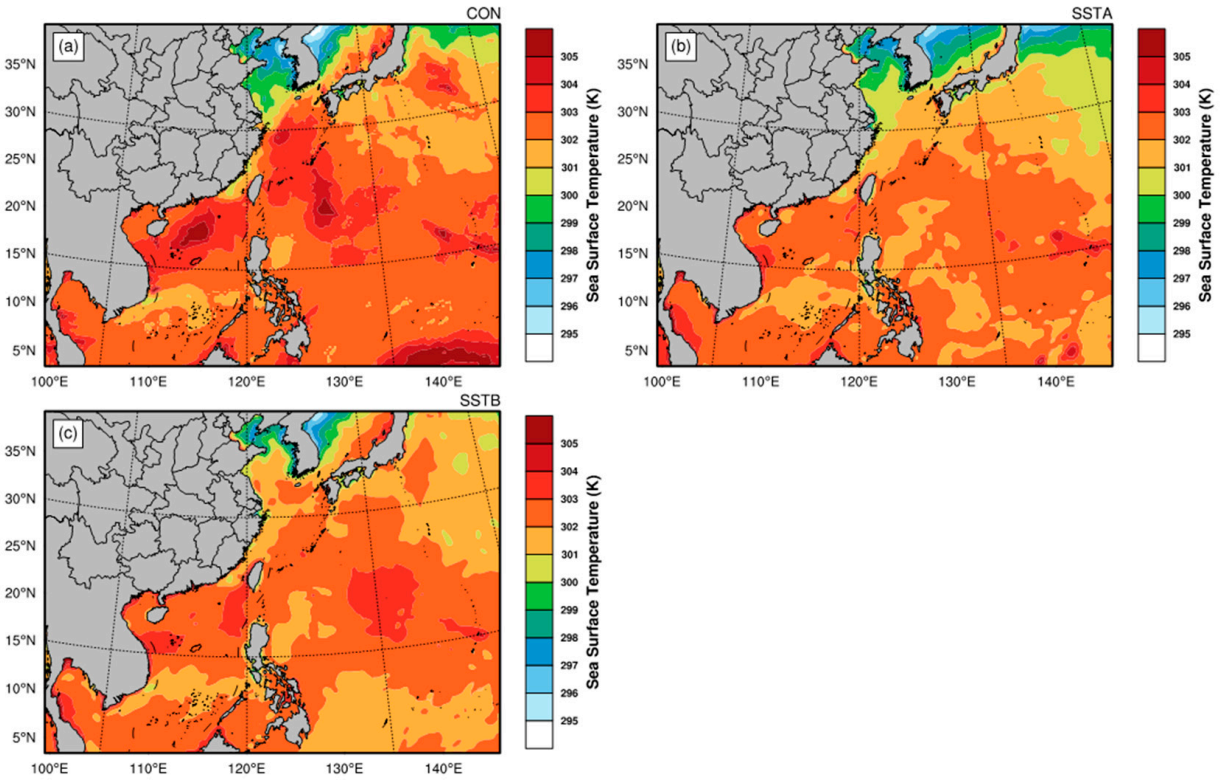


Figure 3. Initial SST (units: K) from (**a**) *CON*, (**b**) SSTA, and (**c**) SSTB.

3.3. Results

With the original SST data in the initial condition, the typhoon track forecast of *CON* is slower and more southeastward than the best track data (Figure 4a). The typhoon turns westward instead of northwestward at 0000 UTC on 1 September. Contrary to *CON*, with the replacement of satellite SST data from FY-4A/B, the typhoon track forecasts are much

closer to the observation. Moreover, the typhoon from SSTB with SST product from FY-4B moved faster than the other two experiments and landed at Zhuhai, while *CON* and SSTA still moved on the ocean at 1200 UTC on 2 September. The track forecast improvement also can be seen clearly in Figure 4b. Even though the track error of all experiments is increasing with the forecast time, SSTB obtains the smallest track error, especially for the last one-day forecast.

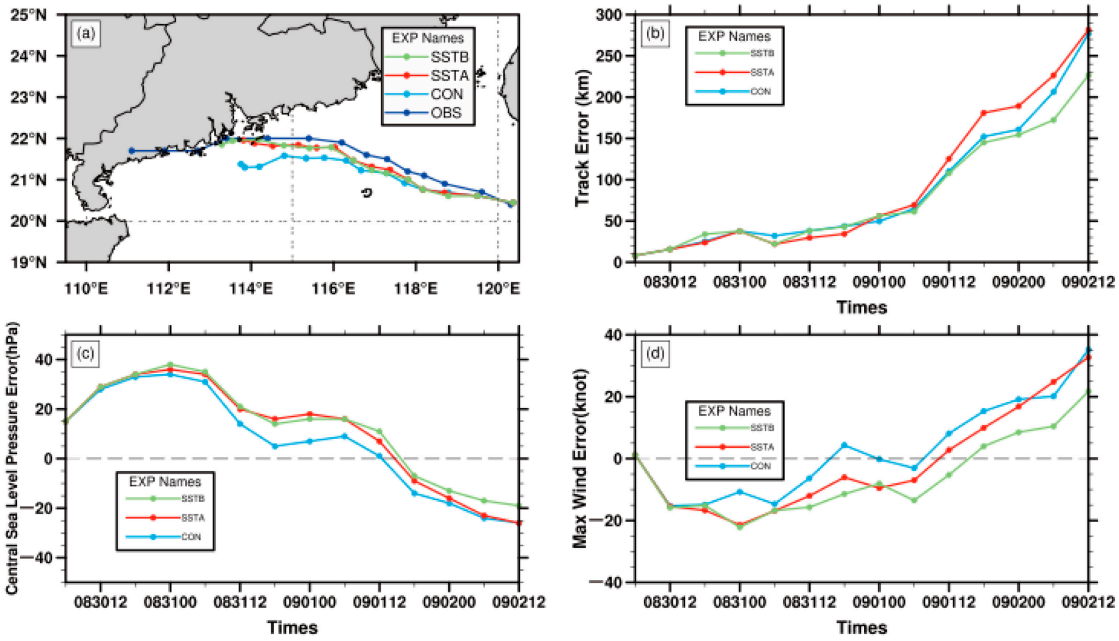


Figure 4. The predicted (**a**) track, (**b**) track errors (units: km), (**c**) CSLP errors (units: hPa), and (**d**) MW errors (units: knot) in *CON* (light blue lines), SSTA (red lines), and SSTB (light green lines) are compared to the JMA best track estimates (blue lines) from 0600 UTC 30 August to 1200 UTC 2 September 2023.

Compared to the track forecast, Figure 4c,d show that all experiments underestimate the intensity of Typhoon Saola when the typhoon is on the sea. During this period, SSTA and SSTB obtain a lager intensity error than *CON*. But, because of the better track forecast in the final 24 h forecast, the intensity forecast from SSTA and SSTB, not only the central sea level pressure (Figure 4c) but also the maximum wind speed (Figure 4d), is smaller than *CON*, especially for SSTB.

The northwestward movement reason can be seen in Figure 5. Following the method described by Zhang et al. (2020) [44], the steering flow is calculated based on winds from 700 to 200 hPa within 3°–5° from the typhoon's center. The steering flow for all experiments is a southeasterly wind with a positive V component and a negative U component, which guides Typhoon Saola to move to Guangdong province. After 0000 UTC on 1 September, *CON*'s V component decreases rapidly and is smaller than in other experiments, which leads to the termination of northward movement. Its U component decreases too, which slows down the speed of moving westward. Combined with the influence of SST (Figure 3), *CON*'s typhoon moves westward to the high SST area instead of northwestward at a slower speed. In the SST replacement experiments, SSTA has a similar large V component as SSTB, which steers the typhoon further northward. But, SSTA obtains a smaller U component than SSTB and *CON*, which decelerates the typhoon and obtains the larger track error in the final forecast time as same as Figure 4b.

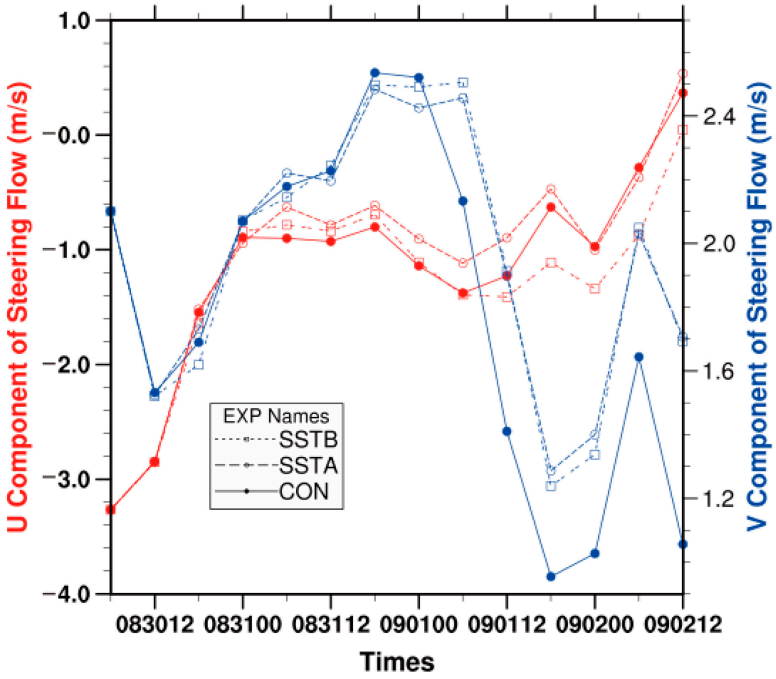


Figure 5. Time series of the U and V components of average steering flow (units: m/s) from 0600 UTC 30 August to 1200 UTC 2 September 2023.

Typhoon Saola finally made landfall in Guangdong and brought heavy precipitation over south Guangdong. The precipitation area extends from Guangxi to Zhejiang, while the precipitation center of more than 200 mm is located at Yangjiang, which can be seen from the station observation scatter plot (Figure 6a) and interpolation shaded plot (Figure 6b). Compared with the observation, all experiments show a much narrower rain band (Figure 6c–e). The experiments miss the precipitation over Guangxi and overpredict in Fujian and Zhejiang. Because of the slower landfall, *CON* brings the smallest heavy rain area in Yangjiang compared to SSTA and SSTB. Meanwhile, SSTB obtains a more accurate position of its precipitation center of more than 200 mm and a better rainfall prediction over north Guangdong and Zhejiang than SSTA.

To quantitatively evaluate the accuracy of precipitation prediction in all experiments, Figure 7 gives the performance diagrams of the 24 h accumulated precipitation for different precipitation thresholds from experiments. The probability of detection (POD), false alarm ratio (FAR), bias score (BIAS), and critical success index (CSI) in the diagrams are defined as follows:

$$\mathrm{POD} = \frac{HIT}{HIT + M}, \mathrm{FAR} = \frac{F}{HIT + F}, \mathrm{BIAS} = \frac{HIT + F}{HIT + M}, \mathrm{CSI} = \frac{HIT}{HIT + F + M} \quad (4)$$

where *HIT*, *F*, and *M* represent hit, false alarm, and miss, respectively. The CSI score indicates the accuracy of the precipitation prediction. It is between 0 and 1, and the larger value means a more precise forecast. The BIAS score indicates whether the precipitation prediction has a tendency to underforecast (BIAS < 1) or overforecast (BIAS > 1) events, and BIAS = 1 is the best score.

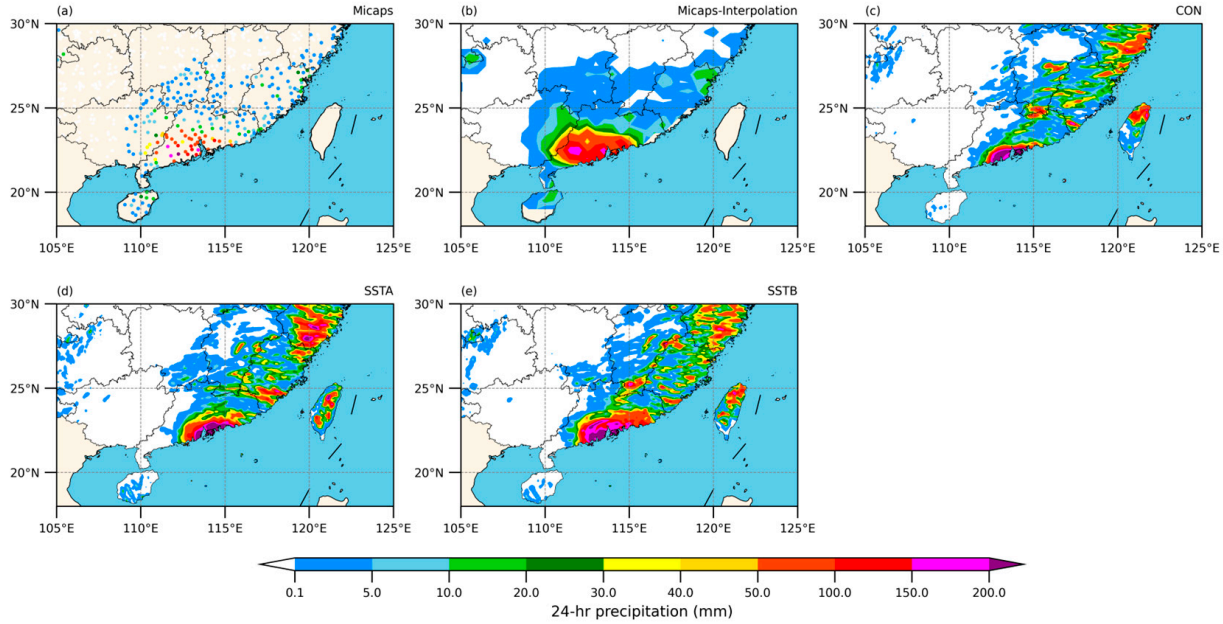


Figure 6. The 24 h accumulated precipitation (units: mm) from 1200 UTC 1 September to 1200 UTC 2 September 2023 of (**a**) the Micaps observation; (**b**) the interpolated Micaps observation with a horizontal resolution of 0.5° × 0.5°; (**c**) *CON*; (**d**) SSTA; and (**e**) SSTB. The dots with different colors in (**a**) represent different accumulated precipitation, as shown in the color bar.

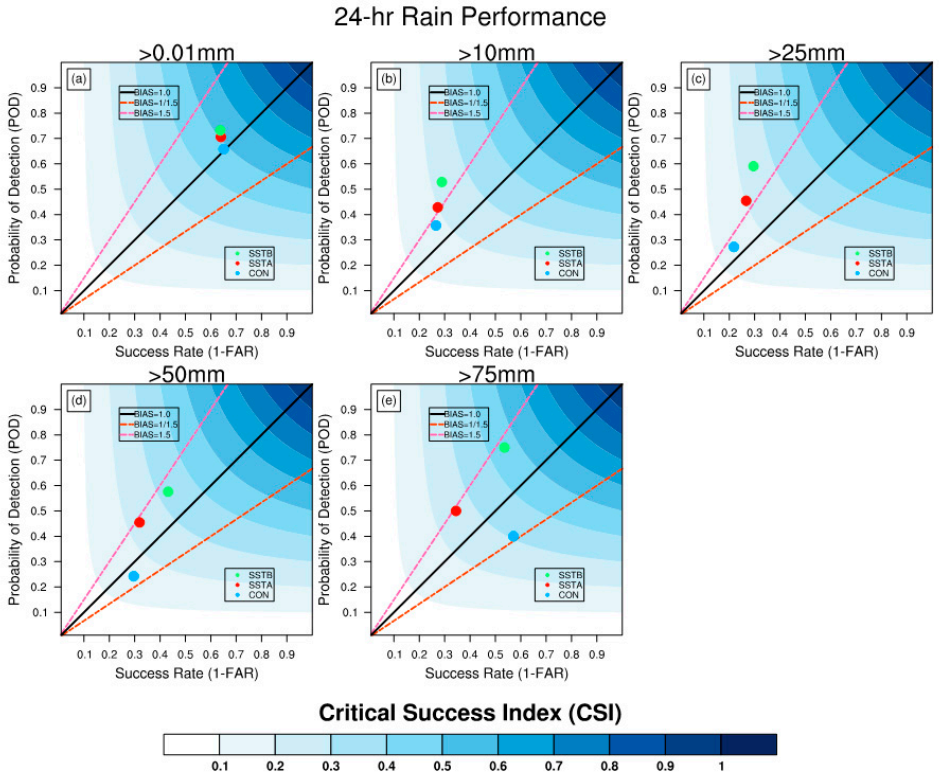


Figure 7. Performance diagram for the 24 h accumulated precipitation for the *CON* (light blue), SSTA (red), and SSTB (light green) with a threshold of (**a**) 0.01 mm; (**b**) 10 mm; (**c**) 25 mm; (**d**) 50 mm; and (**e**) 75 mm from 1200 UTC 1 September to 1200 UTC 2 September 2023.

Figure 7 shows that, except for the threshold of 75 mm, the CSI scores in *CON* are worse than SSTA and SSTB at all precipitation thresholds. This demonstrates the beneficial impact on precipitation prediction when utilizing AGRI SST data as model boundary conditions. Furthermore, the CSI scores in SSTB are the best among all experiments at all thresholds, indicating better precipitation forecast performance using AGRI SST data from FY-4B than from FY4A.

In general, the significant positive impacts can be found in typhoon track prediction and precipitation forecasts when modifying the initial SST with satellite products. Furthermore, SSTB performs better than SSTA. Therefore, the SST product from FY-4B is selected as the initial SST condition in the following AGRI radiance assimilation experiments.

4. Impacts of AGRI Radiance Assimilation on Typhoon Saola Simulation

4.1. Experimental Design

Based on the results of the SST replacement experiments, FY-4B SST data are further chosen to provide the background field for the AGRI radiance data assimilation experiments. To evaluate the effect of AGRI radiance clear-sky/all-sky assimilations on improving atmospheric initial conditions and the combination application of AGRI radiance data and SST data, four assimilation experiments are conducted (Table 2). For all assimilation experiments, a 3 h spin-up run is conducted before performing 3 h data assimilation cycling (DA cycling) from 0900 UTC to 1500 UTC on 30 August 2023. Then, a 69 h deterministic forecast is carried out initialized from the final analysis. The first two experiments, named "CLR" and "CLR + SSTB", assimilate clear-sky AGRI radiances with the background field from the *CON* and SSTB experiments, respectively. The other two assimilation experiments, named "ALL" and "ALL + SSTB", are the same as the first two experiments but assimilate AGRI radiances in all-sky conditions. *CON* and SSTB of SST modification experiments are also compared as benchmarks in this section.

Table 2. The experimental design of AGRI assimilation experiments.

Name	Description
CLR	Clear-sky assimilation with original SST
CLR + SSTB	Clear-sky assimilation with FY-4B SST
ALL	All-sky assimilation with original SST
ALL + SSTB	All-sky assimilation with FY-4B SST

4.2. Results

4.2.1. Impact on the Analysis

Because there is no apparent difference between CLR (ALL) and CLR + SSTB (ALL + SSTB) in terms of the distributions of assimilated observations, CLR and ALL are used for comparison to evaluate the impact and difference between clear-sky and all-sky assimilation for AGRI radiances. Moreover, considering the similarity of channel 9 and channel 10 for the distribution of used observations, channel 9 is selected as the example here.

Figure 8a,b show the distributions of observed BTs after QC from CLR and ALL, respectively. Compared with CLR, more observations with low BTs, which are related to the cloud information, can be effectively assimilated in ALL. Figure 8c illustrates that the number of assimilated pixels at channel 9 in ALL is around five times higher than that in CLR. And, the cloudy pixels assimilated in ALL account for about 75% of the total number of assimilated data. This indicates that the all-sky assimilation approach can obtain more information from cloud-affected areas, which is important for weather system forecasts.

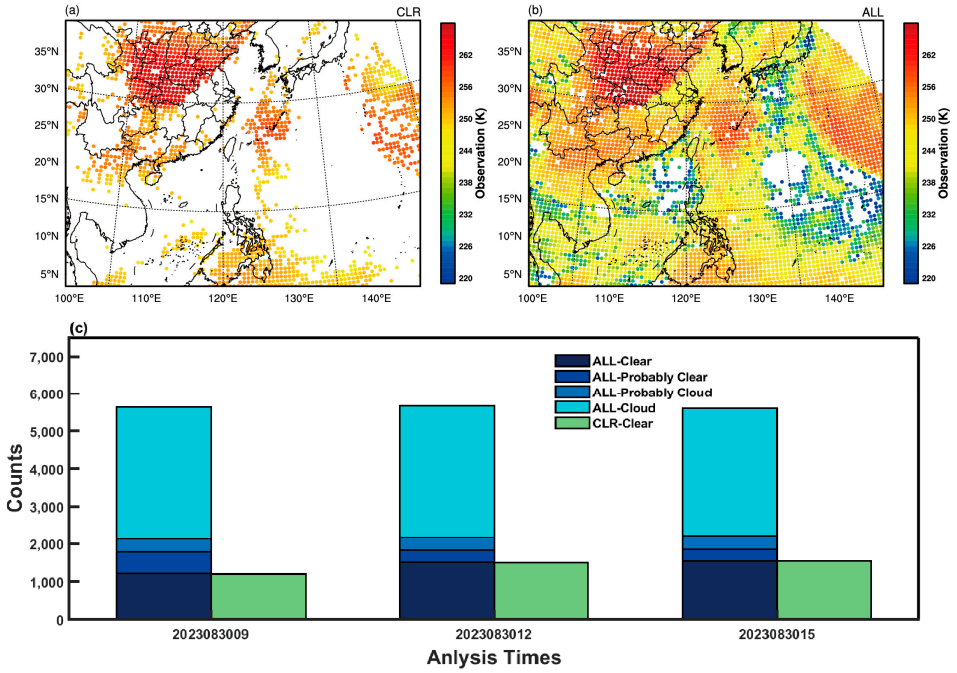


Figure 8. (**a**,**b**) The AGRI observed brightness temperature (units: K) distributions at channel 9 after QC in (**a**) CLR and (**b**) ALL valid at 1500 UTC 30 August 2023. (**c**) The counts of assimilated AGRI observations at channel 9 in ALL and CLR with different cloud mask types every 3 hr from 0900 UTC 30 August to 1500 UTC 30 August 2023.

Focusing on the cloud difference, the cloud top temperatures (*CTTs*) from simulations are selected to evaluate the impacts of AGRI direct assimilation on analysis. Furthermore, to objectively assess assimilation impacts, the improvement parameter (*IP*) of each experiment over *CON* for *CTT* is proposed as IP_{EXP}^{CTT}

$$IP_{EXP}^{CTT} = \frac{RMSE_{CON} - RMSE_{EXP}}{RMSE_{CON}} \times 100\% \quad (5)$$

where the $RMSE_{CON}$ is the *RMSE* from the *CON* used as the benchmark, and $RMSE_{EXP}$ indicates the *RMSE* from the analysis field for each assimilation experiment. The *RMSE* is computed against the AGRI level 2 *CTT* products. Since the diagnostic *CTTs* cover the entire simulation region while AGRI products only cover regions where clouds are detected by the satellite, the *RMSE* is calculated only in regions where both observations and simulations show clouds. In the simulations, sky conditions are determined by the difference between the diagnostic *CTT* and the surface temperature. A difference greater than 8 K indicates a cloudy region, while a difference of less than 8 K indicates a clear region.

Due to the mismatch coverage of *CTT* data, the agreements of sky conditions between simulations and AGRI observations are also evaluated to better understand the impact of assimilation. The sky conditions in the simulation are determined by the above method, while AGRI L2-level *CTT* products are also used for cloud detection in observation. If the value of the AGRI product is not missing, the pixel will be labeled as cloudy. The agreement of sky conditions between simulations and observations is calculated according to the following equation:

$$AGREEMENT = \frac{number\ of\ pxiels\ with\ matched\ sky\ condition}{number\ of\ all\ pixels} \times 100\% \quad (6)$$

And, the *IP* for the sky condition agreement of each experiment over *CON* is defined as IP_{EXP}^{AGR}

$$IP_{EXP}^{AGR} = \frac{AGREEMENT_{EXP} - AGREEMENT_{CON}}{AGREEMENT_{CON}} \times 100\% \quad (7)$$

Positive (negative) values of IPs indicate improvement (degradation), and the larger the values, the better the performance of the experiment over *CON*.

Figure 9 presents the IPs in *CTTs* and agreements on sky conditions for individual experiments. Generally, the results of *CTTs* (Figure 9a) are consistent with the agreements on sky conditions (Figure 9b), but the value for IP_{EXP}^{CTT} is generally larger than the corresponding IP_{EXP}^{AGR}. It can be seen that the IPs in Figure 9 are all positive, with values increasing over time for most experiments. This suggests that the clouds are better analyzed by utilizing AGRI SST data to modify boundary conditions or assimilating AGRI radiances to modify initial conditions. And, the improvements become more pronounced as time progresses. Comparing CLR and ALL with CLR + SSTB and ALL + SSTB, it can be found that experiments with changed SST perform better in *CTT* and sky conditions analyses. And, SSTB also has advantages over *CON*. This suggests that the application of AGRI SST data as WRF ocean boundary conditions can better improve simulations of clouds. In addition, compared with experiments only assimilating clear-sky radiances (CLR and CLR + SSTB), all-sky radiance assimilation leads to greater improvements (ALL and ALL + SSTB), indicating that assimilating more radiances in cloudy regions is beneficial for cloud simulation. Above all, it is clear that the combination application of FY-4 SST and radiance products can significantly improve the analysis filed.

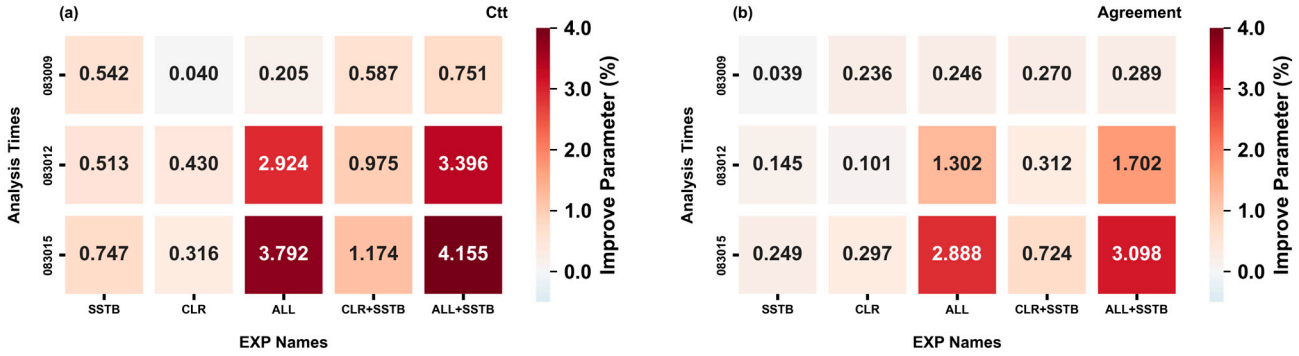


Figure 9. The IPs (units: %) over *CON* of individual experiments every 3 h from 0900 UTC 30 August to 1500 UTC 30 August 2023 in (**a**) *CTTs* and (**b**) agreements on sky conditions.

4.2.2. Impact on the Typhoon Saola Forecasts

From the track forecasts, all forecast results are slower than the best track in general in Figure 10a. Due to the faster movement speed compared to others, ALL has the smallest track error for almost all forecast times among all experiments (Figure 10b). However, it is more south than the best track (Figure 10a). By contrast, through reducing the south track bias, the simulated tracks in experiments (SSTB, CLR + SSTB, ALL + SSTB) with the FY-4B SST product match better with the best track than experiments with original SST (Figure 10a). They also have lower track errors than *CON* and CLR. Moreover, the track error of ALL + SSTB is the lowest among the three SST modification experiments (Figure 10b) due to faster movement speed than SSTB and CLR + SSTB (Figure 10a). In addition, the simulated typhoon in CLR moves slightly faster than SSTB. Nevertheless, the impact of clear-sky assimilation on typhoon track simulation is overall mild. This results in both CLR and CLR + SSTB exhibit little difference from the *CON* and SSTB models for typhoon track simulation. This may be because only a few observations over the sea are assimilated in CLR and CLR + SSTB. Overall, compared with *CON*, ALL + SSTB almost keeps the track error reduction for the whole forecast period and reaches 32% improvement at the last forecast time, while ALL is similar to ALL + SSTB and obtains the

largest reduction at 0000 UTC on 2 September by 41%. SSTB and CLR + SSTB also bring an 18% track error reduction at the end.

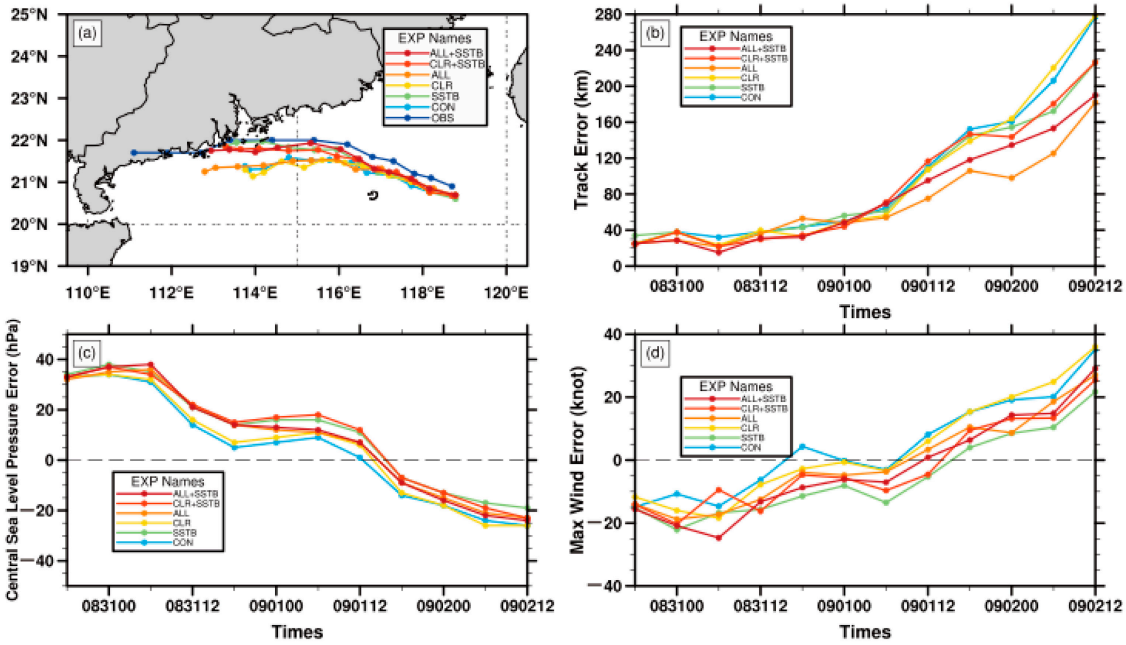


Figure 10. The predicted (**a**) track, (**b**) track errors (units: km), (**c**) CSLP errors (units: hPa), and (**d**) MW errors (units: knot) in *CON* (light blue lines), SSTB (light green lines), CLR (light yellow lines), ALL (orange lines), CLR + SSTB (light red lines), and ALL + SSTB (brown lines) are compared to the JMA best track estimates (blue lines) from 1800 UTC 30 August to 1200 UTC 2 September 2023.

The typhoon intensity for CSLP and MW are shown in Figure 10c,d. The results of CSLP and MW are generally consistent. Overall, typhoon intensities forecast in all experiments are weaker than the best track before 1200 UTC on 1 September. That may be because of the weaker background from NCEP reanalysis, whose intensity is much smaller than the best track data (the CSLP of NCEP reanalysis is 938.36 hPa, while the observation is 920 hPa). Moreover, because satellite products provide cooler SST than the original SST around the area where the typhoon passes through, the typhoon intensity in SST modification experiments is overall weaker than in other experiments before 1200 UTC on 1 September. However, after this time point, compared to *CON*, better performance of the SST modification experiments is shown, as their simulated tracks are closer to observations. Quantitatively, SSTB obtains an average error reduction in CLSP and MW forecasts of around 28% and 50%, while assimilation experiments, except for CLR, gain 10% and 25% error reduction. The highest improvement for ALL + SSTB is at 1800 UTC on 1 September with a 45% and 66% error reduction in CLSP and MW forecasts. Meanwhile, compared with *CON* and SSTB, generally, the clear-sky assimilation has little impact on typhoon intensity prediction in CLR and CLR + SSTB. For the all-sky assimilation approach, ALL and ALL + SSTB have a similar error tendency, which means all-sky assimilation presents a key role in the forecast compared to SST replacement. And, the predicted intensity in ALL + SSTB is stronger than that of SSTB. Therefore, the all-sky assimilation process in ALL + SSTB is beneficial for intensity prediction compared to SSTB before 1200 UTC on 1 September.

The improvements in typhoon track prediction mainly occur after 0600 UTC on 1 September 2023. Therefore, to further analyze the impact of AGRI radiances and SST data on typhoon track prediction, the profiles of the U and V components of steering flows at this time are demonstrated. In Figure 11a, from 450 to 250 hPa, the u component of steering flows in ALL, CLR + SSTB, and ALL + SSTB are lower than in other experiments, leading to faster west movement speeds (Figure 10a). Moreover, the weighting functions for

channels 9–10 also peak around these heights, indicating that the adjustment of the upper steering flows is produced by AGRI radiance assimilation. In terms of the V component of steering flows, all experiments illustrate negative values below 600 hPa, while the values in SSTB, CLR + SSTB, and ALL + SSTB are larger than others (Figure 11b). As a result, these three experiments move further northward than the others. In addition, the values in Figure 11b below 600 hPa for three experiments with replaced SST are similar and differ from the other experiments apparently, indicating that changing the SST mainly affects the movement of the typhoon by adjusting the east–west steering flows at lower layers.

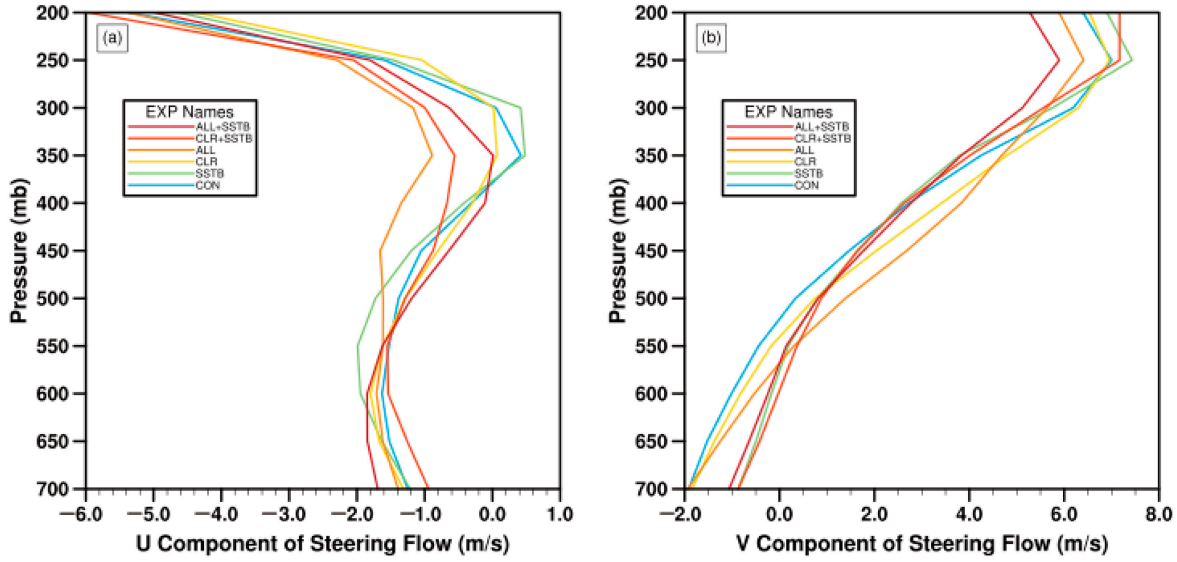


Figure 11. The (**a**) U and (**b**) V components of steering flows (units: m/s) from 700 to 200 hPa with an interval of 50 hPa in individual experiments at 0600 UTC 1 September 2023.

Overall, the AGRI radiance assimilation provides a more accurate u component of steering flow from 450 to 250 hPa, while modifying the original SST with AGRI SST data can effectively adjust the V component of steering flows for the lower atmosphere.

Compared with the precipitation observation (Figure 12a), all simulation experiments overpredict the rainfall in Zhejiang and Fujian. However, with the AGRI data assimilation, CLR (Figure 12c) and ALL (Figure 12d) obtain a better precipitation forecasts in Jiangxi than *CON* (Figure 12b). Moreover, because of more cloudy satellite data assimilation and the higher typhoon moving speed, ALL brings a larger heavy rainfall area in Guangdong than *CON* and CLR, which is closer to observation. This indicates that AGRI data assimilation is good for rainfall prediction, especially with all-sky assimilation.

Replacing SST with the FY-4B retrieval product, SSTB (Figure 12e), and CLR + SSTB (Figure 12f) obtains a larger torrential rain area than *CON* and CLR. ALL + SSTB (Figure 12g) gains a similar southwest–northeast rainband as ALL but a heavier precipitation center and a more accurate forecast in the south of Hunan.

The performance diagrams in Figure 13 also show that, except for CLR, all experiments have advantages over *CON* at all accumulation precipitation thresholds. In the three SST modification experiments, similar CSI scores are observed at all thresholds. However, the BIAS scores in ALL + SSTB are the lowest among the three, with CLR + SSTB following behind. This suggests that the ALL + SSTB rainfall forecast outperforms the other two experiments. Furthermore, the CSI scores for these three experiments at the threshold of 75 mm are higher compared to other experiments (Figure 13e), indicating that the satellite SST data are beneficial for improving heavy precipitation predictions. In ALL, the CSI scores are slightly higher than these three experiments at thresholds of 10, 25, and 50 mm (Figure 13b–d). This could be attributed to the faster typhoon movement speed and the

better precipitation simulation of northwest rainfall areas. Overall, ALL + SSTB has the best forecast skills in the precipitation forecast during the typhoon's landfall.

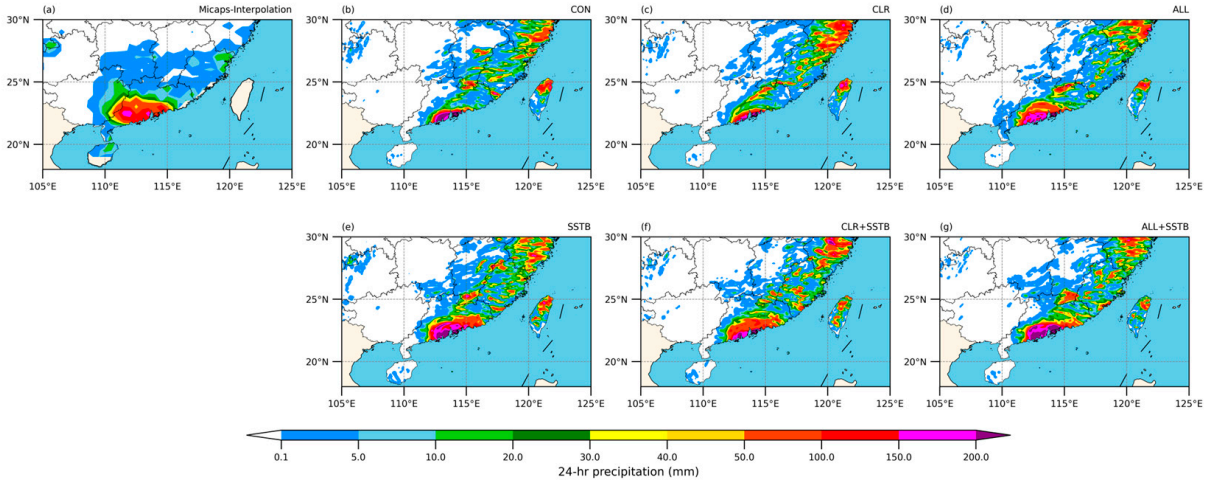


Figure 12. The same as Figure 7 but for (**a**) the interpolated Micaps observation with a horizontal resolution of 0.5° × 0.5°; (**b**) *CON*; (**c**) CLR; (**d**) ALL; (**e**) SSTB; (**f**) CLR + SSTB; and (**g**) ALL + SSTB.

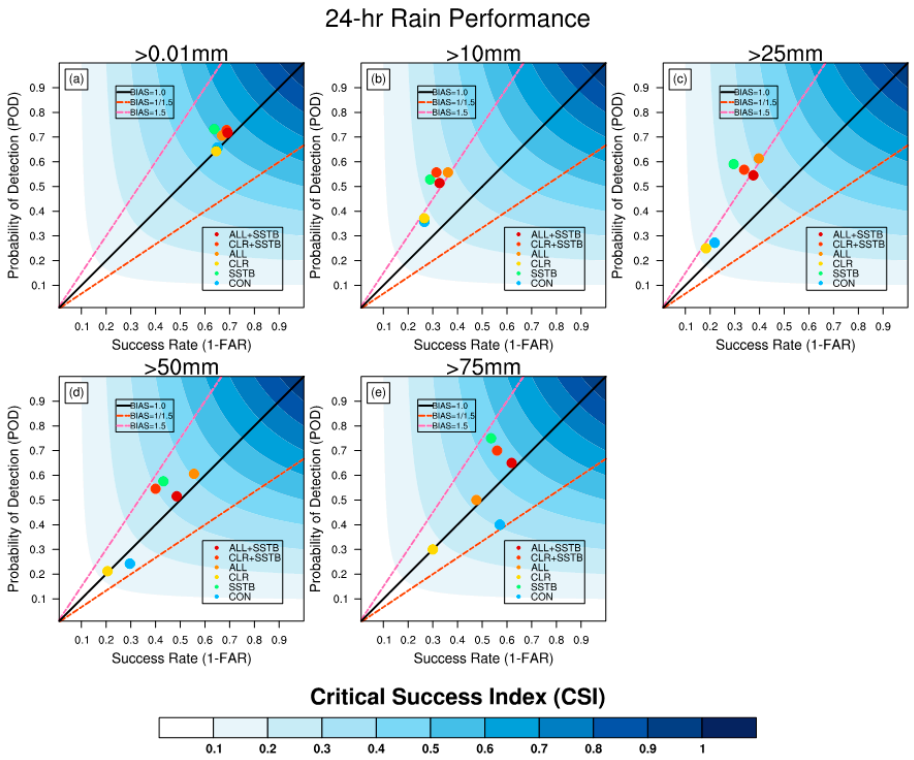


Figure 13. The same as Figure 6 but for *CON* (light blue), SSTB (light green), CLR (light yellow), ALL (orange), CLR + SSTB (light red), and ALL + SSTB (brown) with a threshold of (**a**) 0.01 mm; (**b**) 10 mm; (**c**) 25 mm; (**d**) 50 mm; and (**e**) 75 mm.

5. Conclusions and Discussion

In this study, the combination application of SST and radiance products from FY-4 AGRI are discussed with the AGRI data clear-sky and all-sky assimilation module, which is self-developed in the WRFDA system and operated with the RTTOV model, new bias correction scheme, observation error model, and quality control methods. In order to evaluate the impact of AGRI product application, a case study was conducted for Typhoon Saola in 2023.

Three SST modification experiments were set up firstly to estimate the benefit of the SST product from FY-4A/B. The best track data of JMA, SSTA, and SSTB obviously reduced the south track bias of *CON*. Thus, they produced better track forecasts than *CON*, especially SSTB. Because of a higher SST in *CON* over the sea, *CON* obtained a better intensity forecast before 1200 UTC on 1 September. However, based on the excellent landfall forecast, SSTA and SSTB precipitation forecasts were closer to rainfall observation. Overall, the experiment with SST from FY-4B AGRI was a much better typhoon forecast. Therefore, the SST from FY-4B was chosen to provide the background field for the AGRI radiance data assimilation experiments.

In order to further investigate the impact of the FY-4 AGRI radiance data and the combination application with SST product in the numerical forecast, four AGRI assimilation experiments with clear-sky or all-sky data and different SST conditions are constructed with the new assimilation module. Compared with *CON*, all assimilation experiments obtain positive improvements in *CTT* and sky condition analysis. ALL's *IP* is higher than CLR, which suggests that all-sky assimilation with much cloud information is more beneficial than clear-sky assimilation. In addition, adding the SST's advantage, ALL + SSTB gains the highest *IP*. It indicates that the combination application of FY-4 SST and radiance products, especially with all-sky assimilation, can significantly improve the analysis. For the typhoon forecast, similarly, all experiments with modified SST obtain much northward tracks, which is closer to the best track. With the AGRI assimilation, the typhoon's speed increases, while the all-sky assimilation track error is smaller than clear-sky assimilation. Meanwhile, assimilating all-sky AGRI data can effectively improve the precipitation forecast, which is closer to the rainfall observation.

Overall, the combination application of the FY-4 SST product and radiance product can sensibly improve the typhoon analysis and forecast. It can improve the utilization of FY satellite data and has wild application prospects in numerical prediction. However, this study still is a preliminary study of the combined application of satellite products. It only conducts experiments for one typhoon case. The assimilation and forecast impacts on heavy precipitation and other disastrous weather are also matters worth studying. In addition, because of the lack of a radiative transform coefficient for FY-4B AGRI, only FY-4A AGRI radiance data are assimilated in this study. Therefore, further exploration is also needed for the fusion application of more satellite data from different platforms with different observed purposes in the future.

Author Contributions: Conceptualization, C.Y. and B.S.; methodology, C.Y.; software, B.S.; validation, C.Y. and B.S.; formal analysis, J.M.; writing—original draft preparation, C.Y. and B.S.; writing—review and editing, C.Y. and J.M.; visualization, B.S. All authors have read and agreed to the published version of the manuscript.

Funding: This research was funded by a project supported by the National Natural Science Foundation of China (grant No. 42192553 and No. 41805071) and Postgraduate Research & Practice Innovation Program of Jiangsu Province (KYCX24_1413).

Data Availability Statement: The AGRI radiance data and retrieval data were downloaded from The National Satellite Meteorological Center (NSMC) (https://satellite.nsmc.org.cn/portalsite/Data/DataView.aspx?SatelliteType=1&SatelliteCode=FY4A) accessed on 15 June 2024. The best tracks were from JMA (https://www.jma.go.jp/jma/jma-eng/jma-center/rsmc-hp-pub-eg/besttrack.html) accessed on 10 June 2024. The reanalysis data were obtained from the National Centers for Environmental Prediction (NCEP) (https://rda.ucar.edu/datasets/ds083.3) accessed on 12 June 2024.

Acknowledgments: We would like to express our gratitude to the editors and reviewers for their insightful comments and valuable suggestions on our manuscript. We acknowledge the High-Performance Computing Center of Nanjing University of Information Science & Technology for their support of this work.

Conflicts of Interest: The authors declare no conflicts of interest.

References

1. Emanuel, K. Increasing Destructiveness of Tropical Cyclones over the Past 30 Years. *Nature* **2005**, *436*, 686–688. [CrossRef] [PubMed]
2. Yu, H.; Chen, L. Impact Assessment of Landfalling Tropical Cyclones: Introduction to the Special Issue. *Front. Earth Sci.* **2019**, *13*, 669–671. [CrossRef]
3. Islam, T.; Srivastava, P.K.; Rico-Ramirez, M.A.; Dai, Q.; Gupta, M.; Singh, S.K. Tracking a Tropical Cyclone through WRF–ARW Simulation and Sensitivity of Model Physics. *Nat. Hazards* **2015**, *76*, 1473–1495. [CrossRef]
4. Sun, J.; He, H.; Hu, X.; Wang, D.; Gao, C.; Song, J. Numerical Simulations of Typhoon Hagupit (2008) Using WRF. *Weather Forecast.* **2019**, *34*, 999–1015. [CrossRef]
5. Delfino, R.J.; Bagtasa, G.; Hodges, K.; Vidale, P.L. Sensitivity of Simulating Typhoon Haiyan (2013) Using WRF: The Role of Cumulus Convection, Surface Flux Parameterizations, Spectral Nudging, and Initial and Boundary Conditions. *Nat. Hazards Earth Syst. Sci.* **2022**, *22*, 3285–3307. [CrossRef]
6. Wang, C.; Zeng, Z.; Ying, M. Uncertainty in Tropical Cyclone Intensity Predictions Due to Uncertainty in Initial Conditions. *Adv. Atmos. Sci.* **2020**, *37*, 278–290. [CrossRef]
7. Komaromi, W.A.; Majumdar, S.J.; Rappin, E.D. Diagnosing Initial Condition Sensitivity of Typhoon Sinlaku (2008) and Hurricane Ike (2008). *Mon. Weather Rev.* **2011**, *139*, 3224–3242. [CrossRef]
8. Hsiao, L.-F.; Peng, M.S.; Chen, D.-S.; Huang, K.-N.; Yeh, T.-C. Sensitivity of Typhoon Track Predictions in a Regional Prediction System to Initial and Lateral Boundary Conditions. *J. Appl. Meteorol. Climatol.* **2009**, *48*, 1913–1928. [CrossRef]
9. Bouttier, F.; Kelly, G. Observing-System Experiments in the ECMWF 4D-Var Data Assimilation System. *Q. J. R. Meteorol. Soc.* **2001**, *127*, 1469–1488.
10. Feng, J.; Qin, X.; Wu, C.; Zhang, P.; Yang, L.; Shen, X.; Han, W.; Liu, Y. Improving Typhoon Predictions by Assimilating the Retrieval of Atmospheric Temperature Profiles from the FengYun-4A's Geostationary Interferometric Infrared Sounder (GIIRS). *Atmos. Res.* **2022**, *280*, 106391. [CrossRef]
11. Kieu, C.Q.; Truong, N.M.; Mai, H.T.; Ngo-Duc, T. Sensitivity of the Track and Intensity Forecasts of Typhoon Megi (2010) to Satellite-Derived Atmospheric Motion Vectors with the Ensemble Kalman Filter. *J. Atmos. Ocean. Technol.* **2012**, *29*, 1794–1810. [CrossRef]
12. Liang, J.; Chen, K.; Xian, Z. Assessment of FY-2G Atmospheric Motion Vector Data and Assimilating Impacts on Typhoon Forecasts. *Earth Space Sci.* **2021**, *8*, e2020EA001628. [CrossRef]
13. Eyre, J.R.; Kelly, G.A.; McNally, A.P.; Andersson, E.; Persson, A. Assimilation of TOVS Radiance Information through One-Dimensional Variational Analysis. *Q. J. R. Meteorol. Soc.* **1993**, *119*, 1427–1463.
14. Eyre, J.R.; English, S.J.; Forsythe, M. Assimilation of Satellite Data in Numerical Weather Prediction. Part I: The Early Years. *Q. J. R. Meteorol. Soc.* **2020**, *146*, 49–68. [CrossRef]
15. Shen, F.; Shu, A.; Li, H.; Xu, D.; Min, J. Assimilation of Himawari-8 Imager Radiance Data with the WRF-3DVAR System for the Prediction of Typhoon Soudelor. *Nat. Hazards Earth Syst. Sci.* **2021**, *21*, 1569–1582. [CrossRef]
16. Yang, C.; Liu, Z.; Bresch, J.; Rizvi, S.R.H.; Huang, X.-Y.; Min, J. AMSR2 All-Sky Radiance Assimilation and Its Impact on the Analysis and Forecast of Hurricane Sandy with a Limited-Area Data Assimilation System. *Tellus A Dyn. Meteorol. Oceanogr.* **2016**, *68*, 30917. [CrossRef]
17. Xu, D.; Zhang, X.; Li, H.; Wu, H.; Shen, F.; Shu, A.; Wang, Y.; Zhuang, X. Evaluation of the Simulation of Typhoon Lekima (2019) Based on Different Physical Parameterization Schemes and FY-3D Satellite's MWHS-2 Data Assimilation. *Remote Sens.* **2021**, *13*, 4556. [CrossRef]
18. Honda, T.; Miyoshi, T.; Lien, G.-Y.; Nishizawa, S.; Yoshida, R.; Adachi, S.A.; Terasaki, K.; Okamoto, K.; Tomita, H.; Bessho, K. Assimilating All-Sky Himawari-8 Satellite Infrared Radiances: A Case of Typhoon Soudelor (2015). *Mon. Weather Rev.* **2018**, *146*, 213–229. [CrossRef]
19. Bhate, J.; Munsi, A.; Kesarkar, A.; Kutty, G.; Deb, S.K. Impact of Assimilation of Satellite Retrieved Ocean Surface Winds on the Tropical Cyclone Simulations Over the North Indian Ocean. *Earth Space Sci.* **2021**, *8*, e2020EA001517. [CrossRef]
20. Gray, W.M. The Formation of Tropical Cyclones. *Meteorol. Atmos. Phys.* **1998**, *67*, 37–69. [CrossRef]
21. Mandal, M.; Mohanty, U.C.; Sinha, P.; Ali, M.M. Impact of Sea Surface Temperature in Modulating Movement and Intensity of Tropical Cyclones. *Nat. Hazards* **2007**, *41*, 413–427. [CrossRef]
22. Chang, S.W.; Madala, R.V. Numerical Simulation of the Influence of Sea Surface Temperature on Translating Tropical Cyclones. *J. Atmos. Sci.* **1980**, *37*, 2617–2630. [CrossRef]
23. Emanuel, K.; DesAutels, C.; Holloway, C.; Korty, R. Environmental Control of Tropical Cyclone Intensity. *J. Atmos. Sci.* **2004**, *61*, 843–858. [CrossRef]
24. Vishwakarma, V.; Pattnaik, S.; Chakraborty, T.; Joseph, S.; Mitra, A.K. Impacts of Sea-Surface Temperatures on Rapid Intensification and Mature Phases of Super Cyclone Amphan (2020). *J. Earth Syst. Sci.* **2022**, *131*, 60. [CrossRef]
25. Bongirwar, V.; Rakesh, V.; Kishtawal, C.M.; Joshi, P.C. Impact of Satellite Observed Microwave SST on the Simulation of Tropical Cyclones. *Nat. Hazards* **2011**, *58*, 929–944. [CrossRef]
26. Yang, C.; Li, J. Assessment of FY-3D SST Data on Typhoon In-Fa Simulation. *Atmosphere* **2023**, *14*, 101. [CrossRef]
27. Yang, J.; Zhang, Z.; Wei, C.; Lu, F.; Guo, Q. Introducing the New Generation of Chinese Geostationary Weather Satellites, Fengyun-4. *Bull. Am. Meteorol. Soc.* **2017**, *98*, 1637–1658. [CrossRef]

28. He, M.-C.; Jiang, G.-M. Typhoon Identification and Positioning Using the FY-4A AGRI Thermal Infrared Data. *J. Phys. Conf. Ser.* **2022**, *2400*, 012027. [CrossRef]
29. Wang, G.; Wang, D.; Han, W.; Yin, J. Typhoon Cloud System Identification and Forecasting Using the Feng-Yun 4A/Advanced Geosynchronous Radiation Imager Based on an Improved Fuzzy Clustering and Optical Flow Method. *Adv. Meteorol.* **2019**, *2019*, 5890794. [CrossRef]
30. Shu, A.; Shen, F.; Jiang, L.; Zhang, T.; Xu, D. Assimilation of Clear-Sky FY-4A AGRI Radiances within the WRFDA System for the Prediction of a Landfalling Typhoon Hagupit (2020). *Atmos. Res.* **2023**, *283*, 106556. [CrossRef]
31. Zhang, X.; Xu, D.; Liu, R.; Shen, F. Impacts of FY-4A AGRI Radiance Data Assimilation on the Forecast of the Super Typhoon "In-Fa" (2021). *Remote Sens.* **2022**, *14*, 4718. [CrossRef]
32. Xu, D.; Zhang, X.; Min, J.; Shen, F. Impacts of Assimilating All-Sky FY-4A AGRI Satellite Infrared Radiances on the Prediction of Super Typhoon In-Fa During the Period With Abnormal Changes. *J. Geophys. Res. Atmos.* **2024**, *129*, e2024JD040784. [CrossRef]
33. He, Q.; Hu, X.; Wu, Y. Evaluation and Improvement of FY-4A/AGRI Sea Surface Temperature Data. IEEE J. Sel. Top. Appl. Earth Observations. *Remote Sens.* **2023**, *16*, 267–277.
34. He, Q.; Cui, P.; Chen, Y. Quality Assessment of Operational Sea Surface Temperature Product from FY-4B/AGRI with In Situ and OSTIA Data. *Remote Sens.* **2024**, *16*, 2769. [CrossRef]
35. Yang, C.; Guan, L.; Sun, X. Comparison of FY-4A/AGRI SST with Himawari-8/AHI and In Situ SST. *Remote Sens.* **2023**, *15*, 4139. [CrossRef]
36. Barker, D.M.; Huang, W.; Guo, Y.-R.; Bourgeois, A.J.; Xiao, Q.N. A Three-Dimensional Variational Data Assimilation System for MM5: Implementation and Initial Results. *Mon. Weather Rev.* **2004**, *132*, 897–914. [CrossRef]
37. Parrish, D.F.; Derber, J.C. The National Meteorological Center's Spectral Statistical-Interpolation Analysis System. *Mon. Weather Rev.* **1992**, *120*, 1747–1763. [CrossRef]
38. Shi, B.; Yang, C.; Min, J.; Sha, L. Impact of a New Bias Correction Predictor for FY-4A AGRI All-Sky Data Assimilation on Typhoon Forecast. *JGR Atmos.* **2023**, *128*, e2023JD039063. [CrossRef]
39. Xie, H.; Han, W.; Bi, L. Assimilating FY3D-MWRI 23.8 GHz Observations in the CMA-GFS 4DVAR System Based on a Pseudo All-Sky Data Assimilation Method. *Q. J. R. Meteorol. Soc.* **2023**, *149*, 3014–3043. [CrossRef]
40. Okamoto, K. Evaluation of Radiance Simulation for All-sky Assimilation of Himawari-8 AHI in a Mesoscale NWP System. *Q. J. R. Meteorol. Soc.* **2017**, *143*, 1517–1527. [CrossRef]
41. Dee, D. Variational Bias Correction of Radiance Data in the ECMWF System. In Proceedings of the ECMWF Workshop on Assimilation of High Spectral Resolution Sounders in NWP, Reading, UK, 28 June–1 July 2004; pp. 97–112.
42. Auligné, T.; McNally, A.P.; Dee, D.P. Adaptive Bias Correction for Satellite Data in a Numerical Weather Prediction System. *Q. J. R. Meteorol. Soc.* **2007**, *133*, 631–642. [CrossRef]
43. Skamarock, W.C.; Klemp, J.B.; Dudhia, J.; Gill, D.O.; Liu, Z.; Berner, J.; Wang, W.; Powers, J.G.; Duda, M.G.; Barker, D.M.; et al. A Description of the Advanced Research WRF Model Version 4.3. *Natl. Cent. Atmos. Res.* **2021**, *145*.
44. Zhang, J.; Geng, F.; Yu, X. Study on the calculation method of the steering flow of typhoon Lekima. *J. Meteorol. Sci.* **2020**, *40*, 802–809. (In Chinese)

Disclaimer/Publisher's Note: The statements, opinions and data contained in all publications are solely those of the individual author(s) and contributor(s) and not of MDPI and/or the editor(s). MDPI and/or the editor(s) disclaim responsibility for any injury to people or property resulting from any ideas, methods, instructions or products referred to in the content.